

## Electronic Supplementary Material

# Weak mismatch epitaxy and structural feedback in graphene growth on copper foil

Neil R. Wilson<sup>1</sup> (✉), Alexander J. Marsden<sup>1</sup>, Mohammed Saghir<sup>1</sup>, Catherine J. Bromley<sup>2</sup>, Renald Schaub<sup>2</sup>, Giovanni Costantini<sup>3</sup>, Thomas W. White<sup>3</sup>, Cerianne Partridge<sup>3</sup>, Alexei Barinov<sup>4</sup>, Pavel Dudin<sup>4</sup>, Ana M. Sanchez<sup>1</sup>, James J. Mudd<sup>1</sup>, Marc Walker<sup>1</sup>, and Gavin R. Bell<sup>1</sup>

<sup>1</sup> Department of Physics, University of Warwick, Coventry, CV4 7AL, UK

<sup>2</sup> EaStCHEM School of Chemistry, University of St Andrews, St Andrews, KY16 9ST, UK

<sup>3</sup> Department of Chemistry, University of Warwick, Coventry, CV4 7AL, UK

<sup>4</sup> Sincrotrone Trieste S.C.p.A., Area Science Park, I-34012 Basovizza, Trieste, Italy

Supporting information to DOI 10.1007/s12274-013-0285-y

### 1 EBSD of pure copper foil

Electron backscatter diffraction (EBSD) of a higher purity copper foil (99.999% purity, 0.025 mm thick, Alfa Aesar product number 10950) after graphene growth is shown in Fig. S2. The growth conditions were similar (1000 °C, 20 min anneal etc.) to those used for the foil in Fig. 1 of the main text. However, the resultant grain size and orientations are dramatically different. A random texture is observed with grains typically <100 μm across. The grain sizes and orientations seen in Fig. S1 are consistent with those observed by Wood et al. [S1].

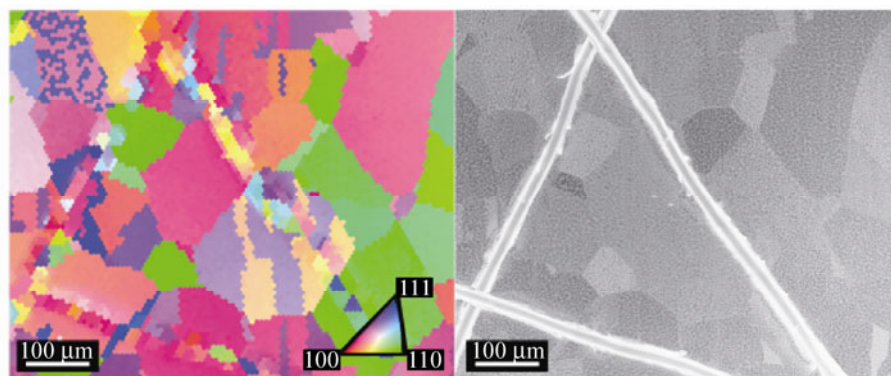


**Figure S1** Electron backscatter diffraction image (left), and SEM secondary electron image (right), of the same region of copper foil (99.999% purity, 0.025 mm thick, Alfa Aesar product number 10950) after graphene growth. The scratches are alignment marks that enable the same area to be readily found for analysis by different techniques.

Address correspondence to Neil.Wilson@warwick.ac.uk

## 2 Effect of foil crystallography on graphene growth rate

A large area SEM map of graphene islands on copper foil (99.5% purity, 0.025 mm thick, Alfa Aesar product number 13382) is given in Fig. S2. Grains within the copper film can be seen, and the dependence of graphene growth rate on local crystallography is apparent from the abrupt changes in graphene island density across the surface. Across grains of the same crystallographic orientation, the graphene island density is uniform.

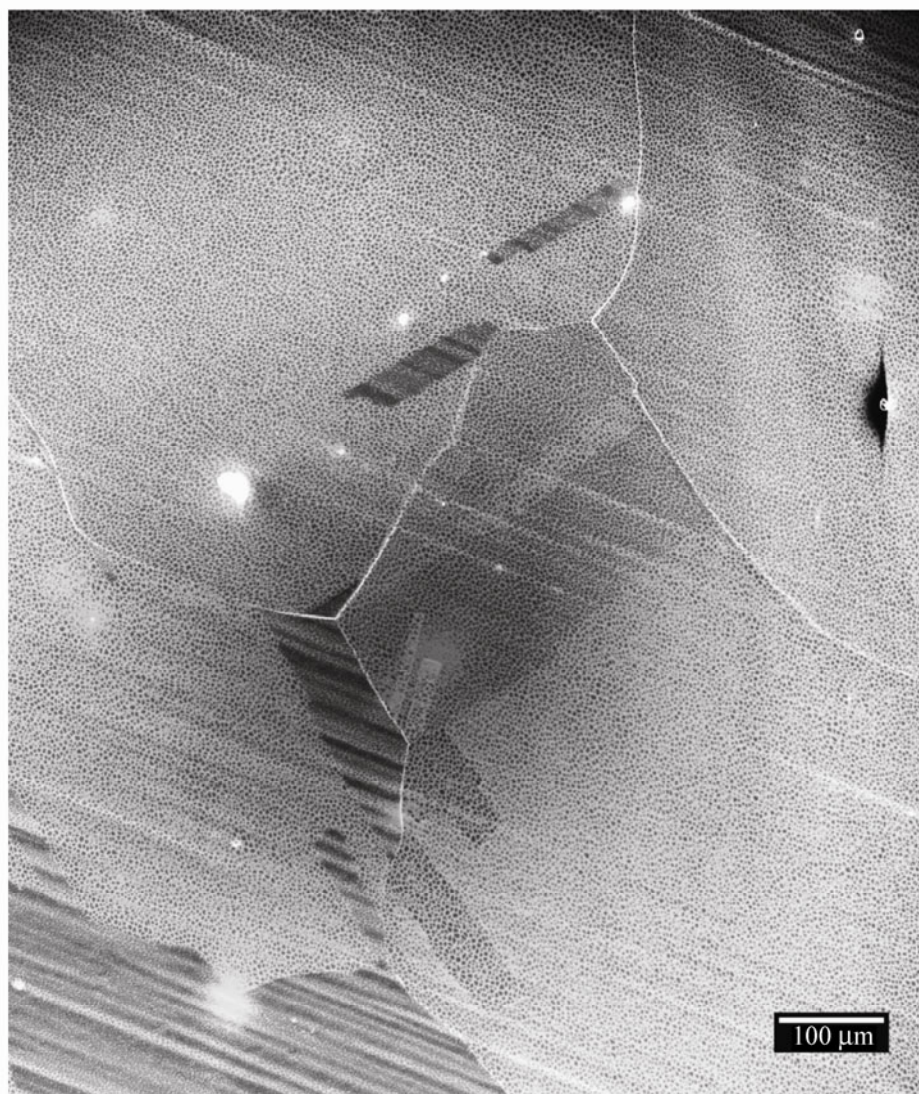


**Figure S2** SEM secondary electron map of graphene islands on copper foil (99.5% purity, 0.025 mm thick, Alfa Aesar product number 13382).

## 3 Correlating frictional force microscopy observations with EBSD measurements

Figure S3 shows the same area of a copper foil sample, after growth of graphene at partial coverage, imaged by SEM, EBSD, and lateral force microscopy (LFM). As shown in Fig. 2 of the main text, there are clear differences in graphene growth on the different copper orientations. The blue stripe of Cu(111) contains a greater density of larger graphene islands than the red/pink which indicates near-(001) copper.

LFM is able to resolve the small ( $\sim 0.1 \mu\text{m}$ ) graphene islands, and these are not apparent on the Cu(111). Note that in the SEM image it is difficult to distinguish the contamination from the small graphene islands, whilst the low-friction signature of graphene makes the distinction obvious in the LFM image.

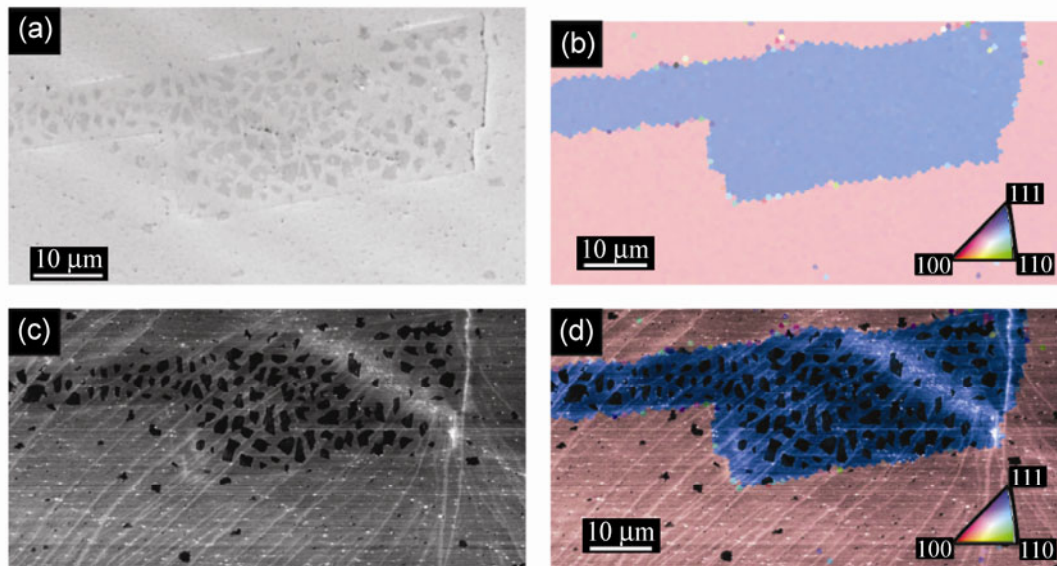


**Figure S3** SEM (a), EBSD (b), and LFM (c), measurements of the same area of copper foil after graphene growth. (d) A composite image formed by overlaying the EBSD (b), on top of the LFM (c).

#### 4 Dependence of surface topography on graphene overlayer

The surface restructuring underneath graphene is most apparent in topographic images where the graphene only partially covers the copper, as in Fig. S4. Regularly orientated terraces and facets are clearly evident, interspersed with smooth regions. The simultaneously acquired friction image shows that the faceted regions are associated with graphene (darker, lower friction), and the smooth (brighter, higher friction) with the absence of graphene.

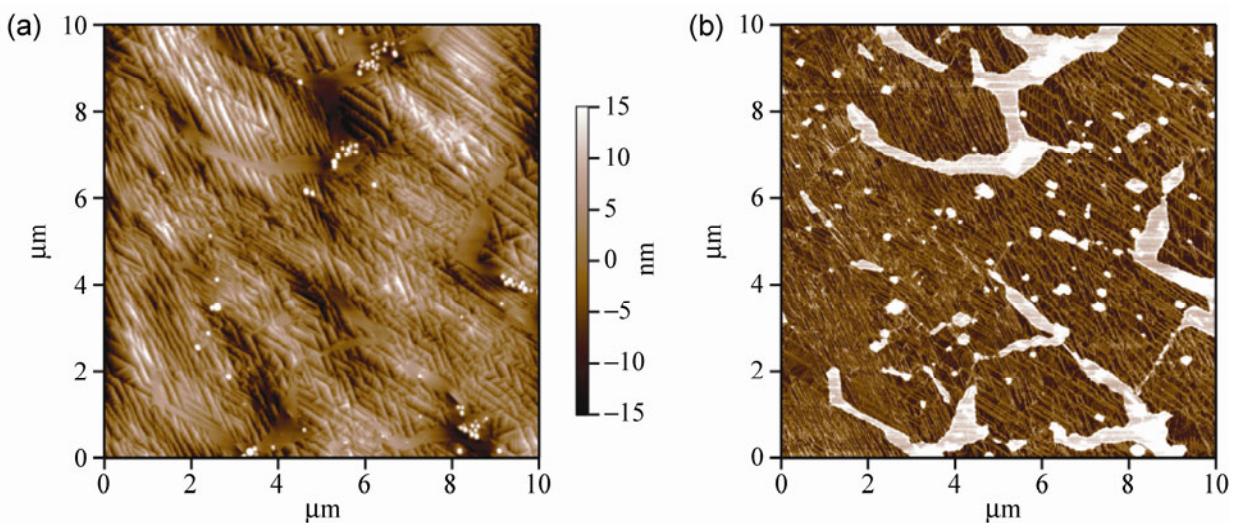


**Figure S4** AFM topography (a), and friction (b), images of graphene on copper foil.

Increasing the growth time or methane flow rate results in full surface coverage of graphene, and in this case the surface faceting is fairly uniform within a given copper grain. The surface restructuring can thus be unambiguously ascribed to the presence of the graphene.

## 5 Raman spectroscopy

For analysis by Raman spectroscopy, graphene was removed from the copper foil. The graphene on copper was spin-coated with poly(methyl methacrylate) (PMMA), then thermal release transfer tape (Nitto Denko) was adhered to the top. The composite structure was placed on the surface of an iron etchant solution until all the copper had dissolved, removed from the etchant and washed thoroughly with deionized water before being dried under a flow of nitrogen.

Raman spectroscopy was performed on a Renishaw inVia Raman microscope at 514.5 nm excitation. As shown in Fig. S5, clear G peaks (at  $\sim 1580\text{ cm}^{-1}$ ) and G'/2D (at  $\sim 2680\text{ cm}^{-1}$ ) were observed with very weak D peaks (at  $\sim 1350\text{ cm}^{-1}$ ). The G'/2D peak here is  $\sim 4$  times more intense than the G peak. The G' peak is well fitted by a single Lorentzian at  $2684\text{ cm}^{-1}$  with width of  $27\text{ cm}^{-1}$ . These metrics all suggest that the resulting graphene is predominantly monolayer with a relatively low concentration of defects [S2, S3].

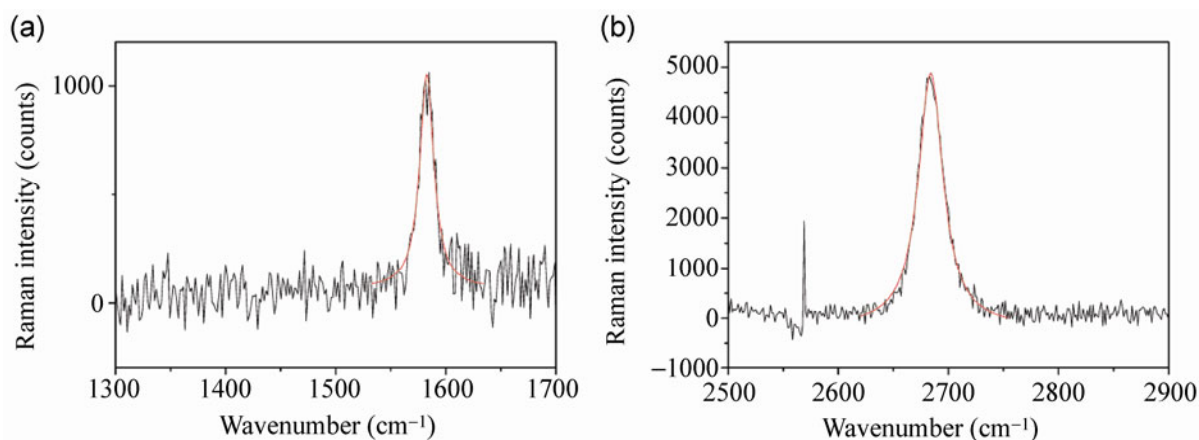


**Figure S5** Raman spectra (black lines) from graphene transferred to PMMA; (a) with the G peak fitted by a single Lorentzian (red line), and (b) with the G'/D peak fitted by a single Lorentzian (red line).

## 6 Further details of the LEED analysis of graphene on copper foil

LEED patterns were obtained for six separate CVD-grown large-grain Cu foil/graphene samples, giving consistent results from sample to sample. The LEED patterns can be understood in more detail by working “backwards” from the IBA-treated clean, graphene-free Cu foil. Figures 5(e) and 5(f) in the main text show clearly a simple square reciprocal lattice whose spacing is consistent with Cu(100). This enables the  $\langle 100 \rangle$  axes of the Cu grains to be identified: to keep the discussion clear we assign [001] to be the horizontal direction on displayed patterns. The {01} spots due to the primitive surface mesh of the fcc (100) surface are at  $45^\circ$  to the  $\langle 100 \rangle$  directions (Fig. S6 red surface mesh, primitive mesh shown as dotted line). Under the annealing conditions in the UHV experiments it is not possible for the bulk grains to reorient, although the surface does indeed restructure, and so the  $\langle 100 \rangle$  directions are fixed for a given grain on the Cu foil. This gives a reliable guide to indexing even complex patterns.

Before IBA, with the graphene still present, all samples showed 12 strong graphene spots, with 12 weak spots usually visible, as discussed in the main text. Here we focus on the Cu substrate spots to relate them to the

surface crystallography and morphology revealed by EBSD and AFM. Facet (00) spots were identified by monitoring spot movement with beam energy and were easy to observe due to their constant position on the screen as the electron energy was changed. The sample LEED movie (in AVI file format) steps through beam energies from 25 to 200 eV, and the non-moving facet spots to the left and right of the electron gun are clearly visible. Although different, weaker facet spots were often observed, the dominant facet spots were always oriented  $26^\circ \pm 2^\circ$  away from the surface normal (00) beam.

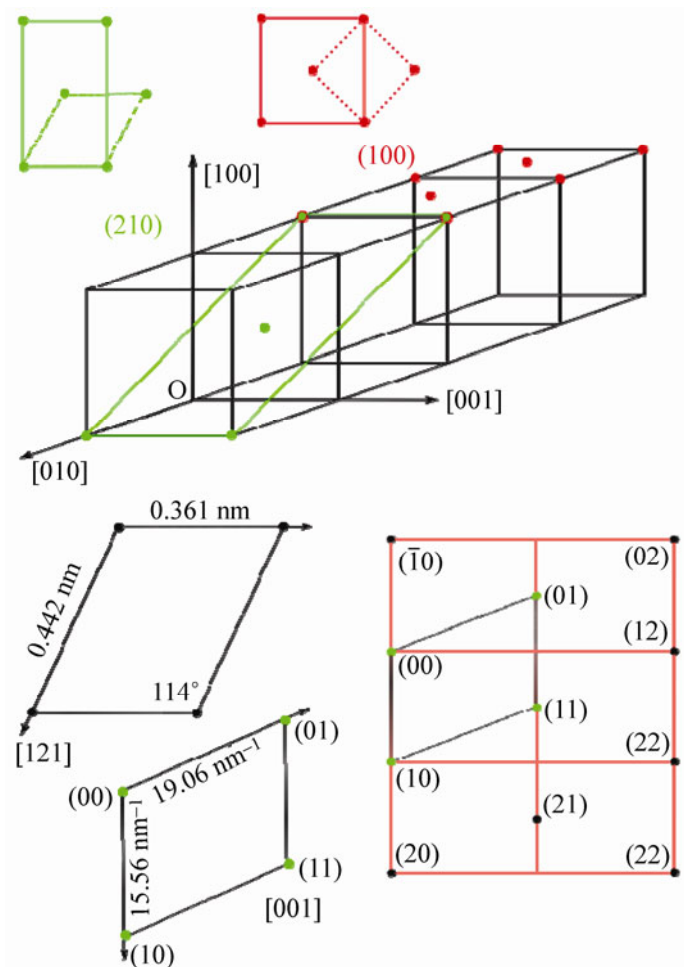


**Figure S6** Real-space and reciprocal space summary for Cu(100) and Cu(210). The top isometric view shows a Cu(210) facet next to a Cu(100) surface. Non-primitive (solid) and primitive (dotted) meshes are shown in green and red respectively.

Of the seven simplest stepped fcc surfaces, i.e., (210), (311), (331), (211), (221), (310) and (410), only the (210) and (311) are angled correctly relative to (100) at  $26.6^\circ$  and  $25.2^\circ$  respectively. However, (311) is tilted towards (111) rather than (110) (see Fig. S7) and so its facet spot would appear at  $45^\circ$  to the main [010] axis of the patterns (Figs. 5(d) and 5(f)). The (210) facet can therefore be identified unambiguously. Other facet spots did appear on some samples but not as reproducibly as the (210), which was clearly the dominant non-(001) face of the foils when graphene was present.

The LEED patterns at higher energy (e.g., 135 eV in Figs. 5(c) and 5(d)) show strong lines of spots parallel to the main [010] axis. Even such a complex pattern can be explained by simulating LEED spot positions for a combination of (210) facets and (100) surfaces, at a given beam energy. Figure S8 shows the real space surface

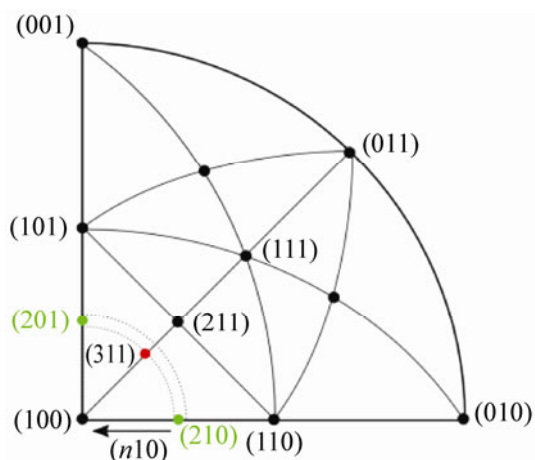


**Figure S7** Simplified stereographic projection of relevant surface planes for an fcc crystal. The dotted lines represent the main facet angle to (100) of  $26^\circ \pm 2^\circ$  identified by LEED.

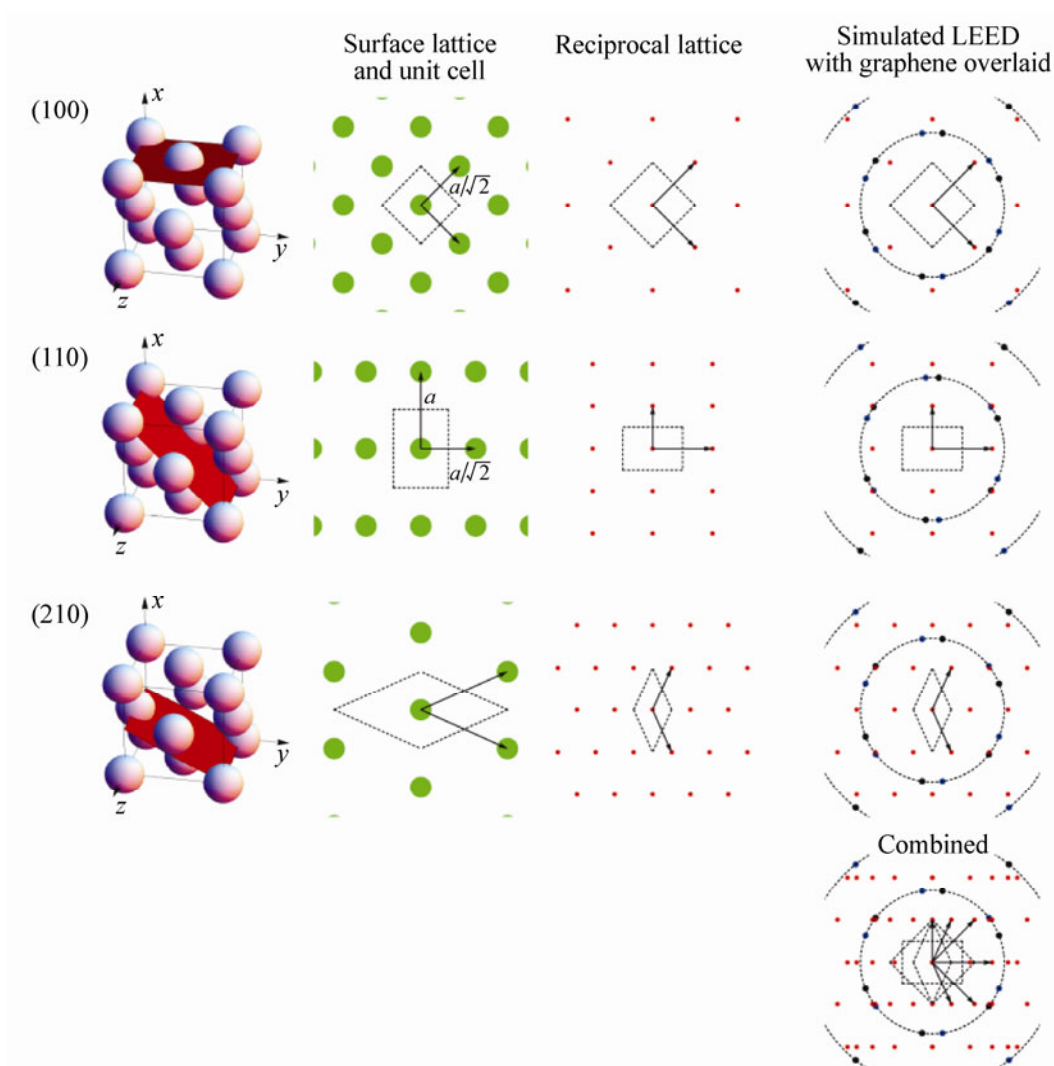


**Figure S8** Real space and reciprocal lattices of the Cu(100), Cu(110) and Cu(210) copper surfaces. The final column shows the respective reciprocal space lattices overlaid with the two characteristic orientations of graphene and dashed lines indicating the expected reciprocal lattice spacings for graphene of any orientation.

lattice for Cu(100), Cu(110) and Cu(210) along with their respective reciprocal lattice. The final column overlays the graphene reciprocal lattice, with the two characteristic orientations of graphene and dashed lines indicating the expected reciprocal lattice spacings for graphene of any orientation. On the top row of Fig. S9 is an experimental LEED pattern showing a complex array of spots. On the bottom row this experimental pattern is overlaid first by the Cu(100) with graphene spots alone. This is clearly not sufficient to explain the data. The second image on the bottom row overlays the predicted Cu(210) pattern aligned to the Cu(210) facet, the match to the experimental LEED spots is clear. The other Cu(210) facet, third image, is less distinct but some spots can be assigned to it. Combining them, the final image, provides almost complete indexing of the experimental LEED pattern (although the effects of aberrations in the LEED optics are apparent at the edges of the screen). The importance of Cu(210) faceting is thus clear. Note that the greater angle of the Cu(110) facet means that it is not possible from this data to distinguish whether it is present on these copper foil samples.

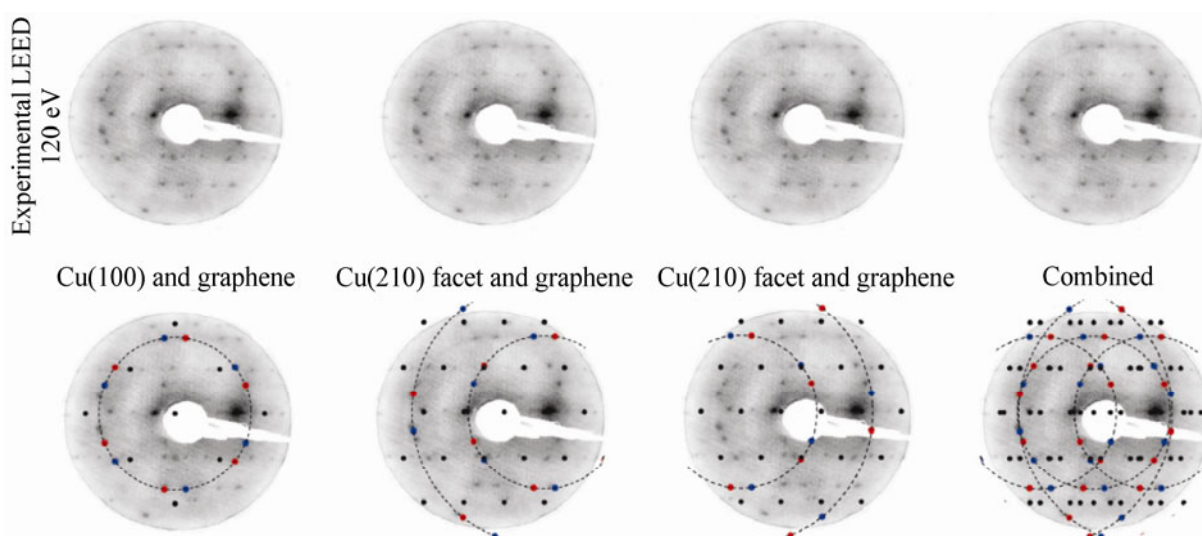


**Figure S9** (top) Experimental LEED pattern from graphene on copper foil. (bottom) The same experimental image overlaid with simulated LEED patterns as labeled.

It should be noted that (probably due to the cold-rolling manufacture of the foils) the  $\langle 100 \rangle$  directions were quite consistently aligned across a given 5–7 mm wide sample. However, it was difficult to avoid some wrinkling of the foils when mounting them on UHV sample plates. This added the complication of macroscopic misalignment of the surface which confounded the LEED patterns greatly where the beam lay on a wrinkled area. Nonetheless, on nearly every sample studied it was possible to find substantial areas of the foil giving clear LEED patterns such as that shown in Fig. 5. We observed these patterns on many samples and using three different LEED systems. It is also worth re-emphasizing the statistical significance of the LEED patterns. An area of ca. 1 mm radius (the approximate LEED beam size) contains some  $10^5$  graphene grains of diameter  $\sim 3 \mu\text{m}$ . The distinct spots patterns for graphene observed in these LEED patterns imply that the great majority of these grains must be well aligned. Such a pattern could not be observed if the orientation of the graphene grains was random.

Figure S10 shows raw LEED data for three different samples than shown in the main text or Fig. S9. The top row (a) shows a sample being moved under the LEED beam. The graphene spots are clearly visible at the edge of the pattern and several weaker Cu facet spots appear around the electron gun. On moving 0.5 mm across a single grain there is almost no change in the LEED pattern. After a further lateral move of 2 mm, the LEED beam encounters a wrinkle and/or a second grain, and the pattern becomes more complex with higher

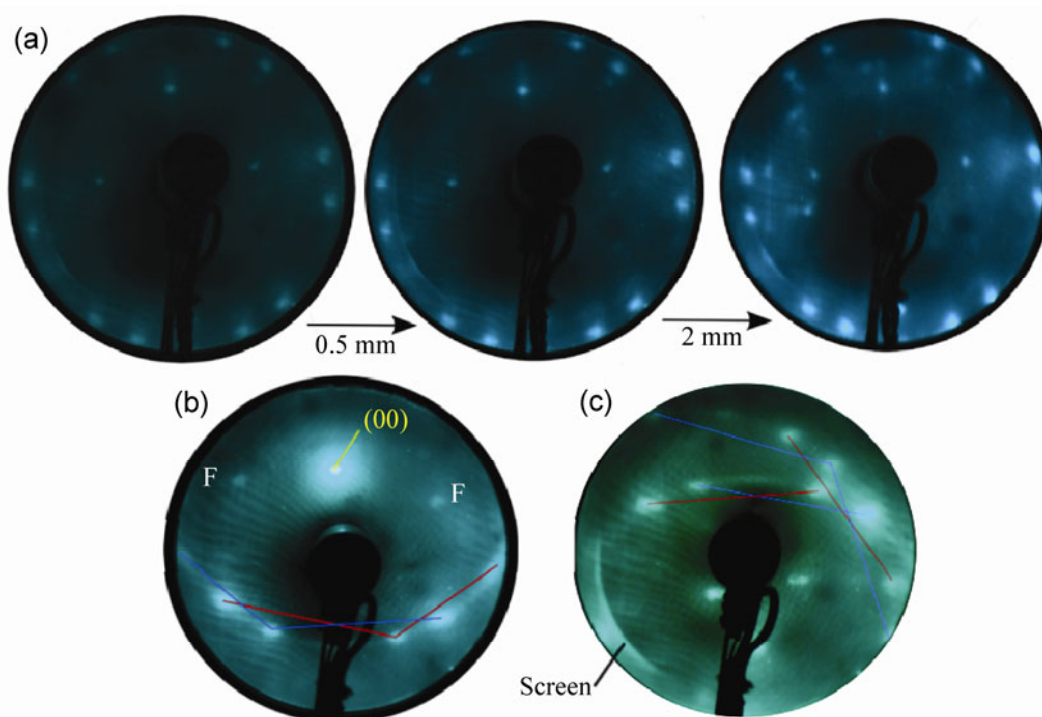


**Figure S10** Further examples of LEED images from different graphene/Cu samples. The top row (a) shows raw LEED images at 76 eV and the effect of moving the sample laterally under the LEED beam. Below, (b) shows a different sample at 55 eV with the surface normal tilted relative to the LEED optics (graphene hexagons, lateral facet spots and (00) beam are highlighted). Image (c) is 60 eV from another sample in a “wrinkled” region showing at least 2 graphene arcs. The smooth arc in these images, labeled “Screen” in (c), is an artifact of the channel plate LEED screen.

background intensity, although the principal graphene spots are still very strong. This behavior was typical and is consistent with a  $\sim 1$  mm LEED beam size and Cu grain size of several mm. Some of the samples showed only minor variations in LEED pattern quality across most of the foil. Figure S10(b) gives an example from another different sample with the surface normal tilted relative to the LEED optics. For this region of this sample the rotational ordering of the graphene overlayer is a little weaker, as evidenced by the stronger intensity between the graphene spots, but the principal spots are still paired and strong. Image (c) is a third different sample in a more wrinkled region. Patterns like this are harder to interpret unambiguously but (c) shows quite clearly spot pairs in at least 2 graphene arcs in different orientations. Note that the images in Fig. S10 were taken using a low-current channel plate-type LEED optics with a smaller subtended angle than a standard system (as shown in the main text and Fig. S9). Smooth arcs near the edge of the screen are an artifact of the channel plate. No electron beam damage was ever noticed even with standard beam currents.

An important final note concerns the disappearance of the facet spots after IBA. Figure S11 shows AFM images of a graphene on copper sample after IBA. Figure S11(a) is from the top surface, i.e., the surface that was exposed to the ion bombardment, whilst Figure S11(b) is from the bottom surface, i.e., it had the same annealing without any ion bombardment. The top surface is smooth (note differences in height scale) without evidence of faceting, whilst the bottom surface which is still graphene coated has retained the characteristic faceting. Amorphization of the copper surface by the ion sputtering process combined with the very high mobility of Cu surface atoms at 550 °C is sufficient to explain the decay of the facets, observed both in LEED and AFM. This process is unambiguous and repeatable, and underlines the role of graphene in stabilizing the facets.

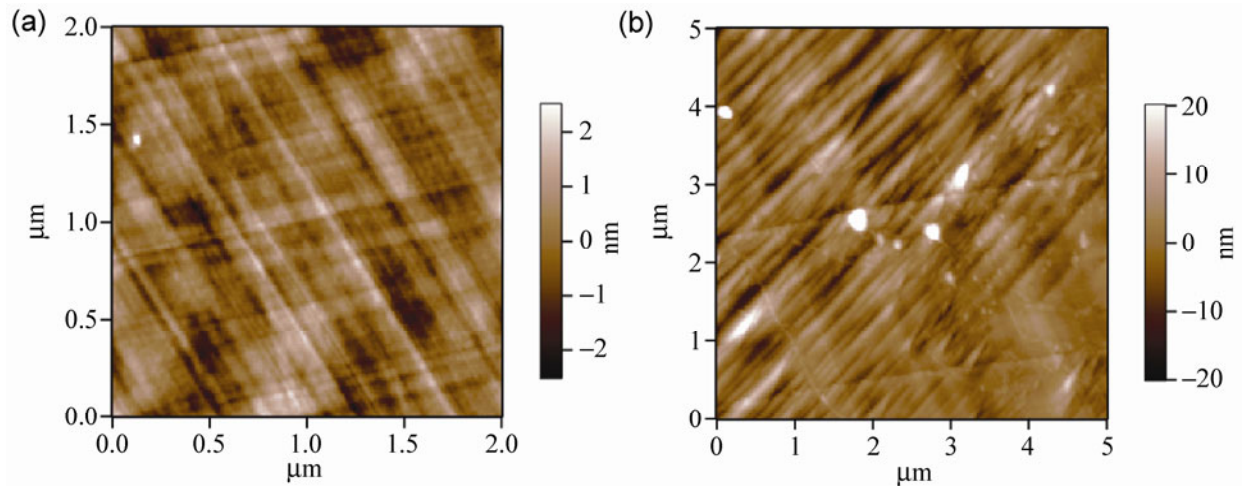


**Figure S11** AFM topography images of a graphene on copper foil sample after ion bombardment and annealing. (a) From the top surface and shows a smooth surface with no evidence of faceting or of graphene. (b) From the bottom surface (i.e., not exposed to the ion bombardment and hence retaining the graphene, but subject to the annealing) and retains the characteristic faceting. Note the difference in height scales.

## 7 Further DF-TEM characterization

Figure S12 shows the two dark-field TEM images, taken of the two different orientations of graphene that are then merged to form a color composite image.

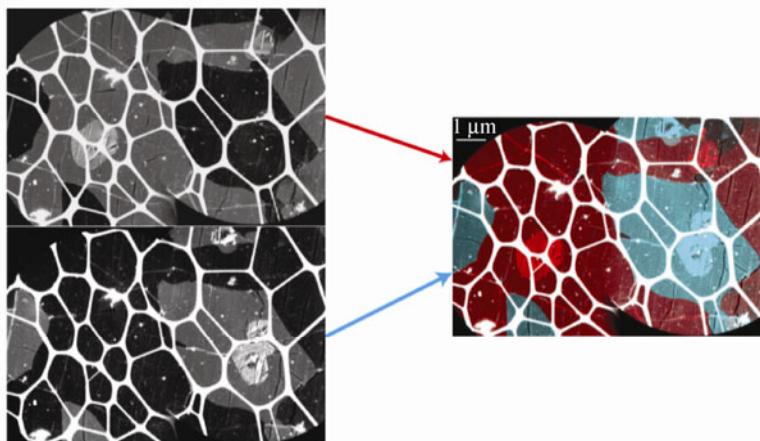


**Figure S12** Merging dark-field TEM images to create a composite color image as in Fig. 6.

Figure S13 shows line profiles through the diffraction patterns in Figs. 6(c) and 6(e) as marked. The line profile in (f) from the region highlighted in (c) shows that the “inner hexagon” of diffraction spots, corresponding to  $hk = 10$ , are less intense than the “outer hexagon”,  $hk = 11$ ; the ratio of intensities here is  $I_{11}/I_{10} = 1.3$ . A similar analysis of (e)/(g) gives  $I_{11}/I_{10} = 0.6$ . Assuming AB stacking, the predicted ratio of electron diffraction intensities at 200 kV for a mono-layer of graphene is  $I_{11}/I_{10} = 1.1$ , and for a bi-layer  $I_{11}/I_{10} = 0.28$  (ignoring lattice vibrations) [S4]. The diffraction patterns, combined with the intensities in the dark-field image, thus identify the regions as mono-layer and AB stacked bi-layer.

A composite dark-field TEM map of another area of graphene is given in Fig. S14, with (b) and (c) showing diffraction patterns from the selected areas. Figure S14(c) shows two orientations of graphene rotated approximately  $30^\circ$  to each other. Examining the separate dark-field images that form the composite shows that the two layers are on top of one another, i.e., that in this instance the second layer is turbostratic. In most cases,

dark-field TEM imaging and electron diffraction show that where more than one layer of graphene is present the second graphene layer is either AB stacked to the first or rotated 30° relative to it.

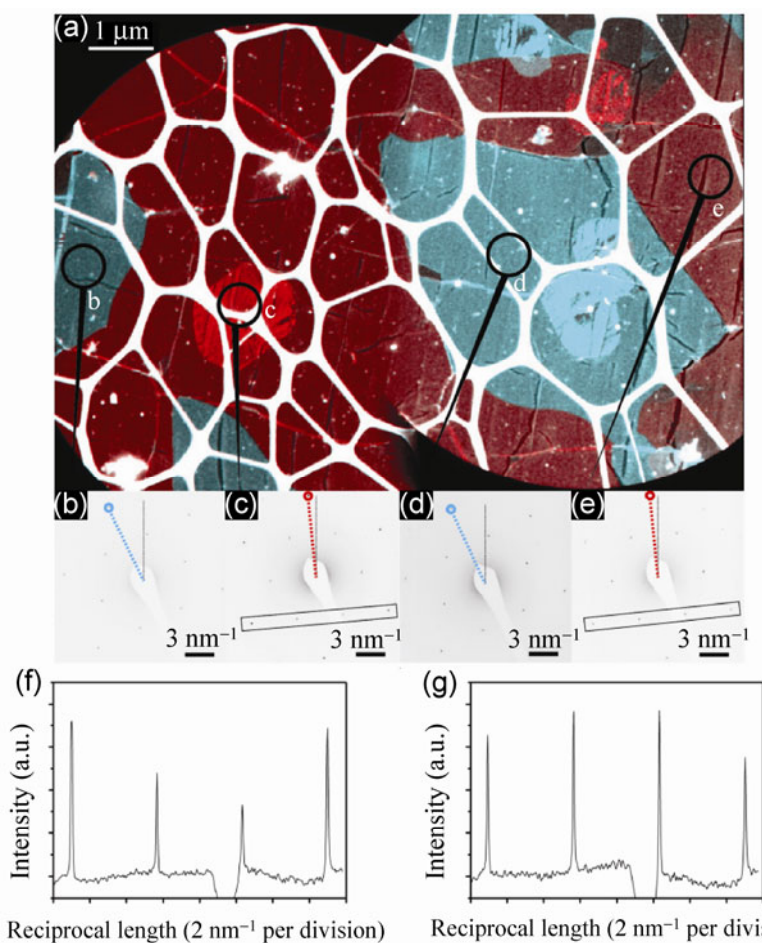


**Figure S13** A reproduction of Fig. 7 from the main text with additional line profiles, as marked, from diffraction patterns (c) and (d) given in (f) and (g), respectively.

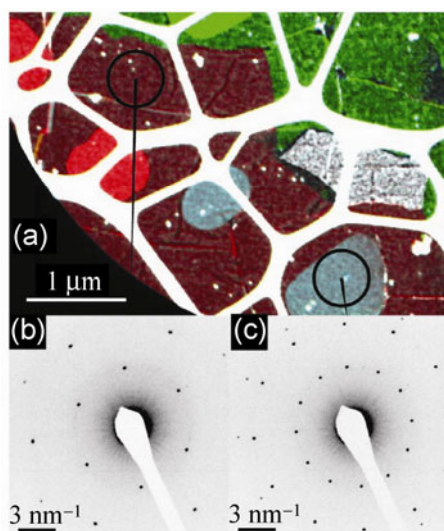


**Figure S14** (a) Composite dark-field TEM of graphene film on lacy carbon support. Selected area electron diffraction patterns are given in (b) and (c) from the regions indicated.

## 8 Predicted angles in the mismatch epitaxy of graphene on single crystal Cu(110)

The expected angle between graphene orientations on Cu(110) surface can be calculated from the reciprocal lattice as shown in Figs. S1–S3. The angle between the two orientations is given by  $\phi = 120 - \theta$ , where  $\theta = 2 \tan^{-1}(\sqrt{2}) = 109.47^\circ$ . This gives an expected angle of  $\phi = 10.53^\circ$ .

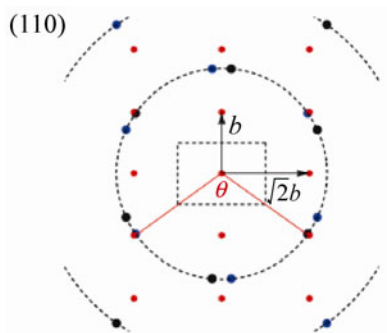


**Figure S15** Schematic view of the LEED pattern from graphene on Cu(110).

## References

- [S1] Wood, J. D.; Schmucker, S. W.; Lyons, A. S.; Pop, E.; Lyding, J. W. Effects of polycrystalline Cu substrate on graphene growth by chemical vapor deposition. *Nano Lett.* **2011**, *11*, 4547–4554.
- [S2] Malard, L. M.; Pimenta, M. A.; Dresselhaus, G.; Dresselhaus, M. S. Raman spectroscopy in graphene. *Phys. Rep.* **2009**, *473*, 51–87.
- [S3] Pimenta, M. A.; Dresselhaus, G.; Dresselhaus, M. S.; Cancado, L. G.; Jorio, A.; Saito, R. Studying disorder in graphite-based systems by Raman spectroscopy. *Phys. Chem. Chem. Phys.* **2007**, *9*, 1276–1290.
- [S4] Wilson, N. R.; Pandey, P. A.; Beanland, R.; Rourke, J. P.; Lupo, U.; Rowlands, G.; Roemer, R. A. On the structure and topography of free-standing chemically modified graphene. *New J. Phys.* **2010**, *12*, 125010.